

ARTICLE OPEN

Pressure-induced superconductivity in topological semimetal NbAs₂Yupeng Li¹, Chao An², Chenqiang Hua¹, Xuliang Chen¹, Yonghui Zhou², Ying Zhou², Ranran Zhang², Changyong Park³, Zhen Wang^{1,4}, Yunhao Lu⁴, Yi Zheng^{1,5}, Zhaorong Yang^{2,5} and Zhu-An Xu^{1,4,5}

Topological superconductivity with Majorana bound states, which are critical to implement nonabelian quantum computation, may be realized in three-dimensional semimetals with nontrivial topological feature, when superconducting transition occurs in the bulk. Here, we report pressure-induced superconductivity in a transition-metal dipnictide NbAs₂. The emergence of superconductivity is not accompanied by any structural phase transition up to the maximum experimental pressure of 29.8 GPa, as supported by pressure-dependent synchrotron X-ray diffraction and Raman spectroscopy. Intriguingly, the Raman study reveals rapid phonon mode hardening and broadening above 10 GPa, in coincident with the superconducting transition. Using first-principle calculations, we determine Fermi surface change induced by pressure, which steadily increases the density of states without breaking the electron–hole compensation. Noticeably, the main hole pocket of NbAs₂ encloses one time-reversal-invariant momenta of the monoclinic lattice, suggesting NbAs₂ as a candidate of topological superconductors.

npj Quantum Materials (2018)3:58; doi:10.1038/s41535-018-0132-1

INTRODUCTION

There have been various proposals in search of quasiparticle excitations of Majorana fermions (MFs) in solids, which are the subject of both fundamental research and error-tolerant topological quantum computing.^{1,2} Superconductor–topological insulator (TI) heterostructures turn the surface Dirac fermions of topological insulators (TIs) into *p*-wave-like Cooper pairs.³ Majorana zero modes by this superconducting proximity approach have been observed in vortices by scanning tunneling microscopy in Bi₂Te₃/NbSe₂ heterostructures.^{4,5} Superconducting proximity effects may also create MFs in semiconducting nanowires with strong spin–orbital coupling,^{6,7} or in ferromagnetic atomic chains.⁸ Alternatively, chiral Majorana edge states are expected in two-dimensional (2D) chiral topological superconductors, consisting of a topological insulator in proximity to an *s*-wave superconductor.^{9–12} It is intriguing that superconducting phase transitions are widely observed in many topological materials when high pressure is applied, such as type II Weyl semimetals of MoTe₂¹³ and WTe₂,^{14,15} Dirac semimetals of Cd₃As₂¹⁶ and ZrTe₅,¹⁷ and topological insulators of Bi₂Se₃,¹⁸ Bi₂Te₃,¹⁹ and Sb₂Te₃.²⁰ Recently tip-induced superconductivity (SC) has attracted much attention because it could offer a new platform to study topological SC (TSC) in Dirac²¹ and Weyl semimetals.²² Charge carrier doping is the another effective method to induce TSC in topological insulators such as in Cu_xBi₂Se₃²³ and Sr_xBi₂Se₃.²⁴ The experimental observations strongly suggest the feasibility to realize TSC^{25,26} in novel topological materials with nontrivial topological features. However, before the emergence of SC, most

of these topological compounds undergo structural phase transitions, which usually change the topological states.

Very recently, transition-metal dipnictides of the MPn₂ family,^{27–33} where M represents Mo, Nb, or Ta atom, and Pn is As or Sb atom, respectively, generate a wide interest as a new prototype of topological semimetals with extremely large magnetoresistance (XMR). When spin–orbital coupling is included, the band anticrossing in MPn₂ between the *M*-*d*_{xy} and *M*-*d*_{x²-y²} orbitals along the *l*-*l*' direction are fully gapped,³⁴ resulting in weak topological insulator invariants of $\mathbb{Z}_2 = [0; 111]$.^{28,31,35} Another interesting point in the MPn₂ family is that magnetic field could induce Weyl points.³⁶ With its monoclinic lattice (Space group No. 12), which is normally stable under very high pressure,^{16,17} it is tempting to study the physical properties of MPn₂ under high pressure.

In this work, we report pressure-dependent transport measurement and structure evolution in NbAs₂, using the diamond-anvil-cell (DAC) technique to continuously tune the electronic structure. Superconducting transition has been successfully observed at 12.8 GPa with a critical temperature (*T*_c) of 2.63 K. Further increase in pressure gradually suppresses *T*_c, which disappears completely at 27.9 GPa when bad metal (BM) behavior dominates below the helium temperature. Using high-pressure X-ray diffraction (XRD) and Raman scattering, we confirm that there is no structural phase transition up to the maximum experimental pressure of 29.8 GPa, which implies that the topological state maybe remain undisturbed under high pressure. Intriguingly, the electron–hole compensation in NbAs₂ changes little even in the superconducting region, as suggested by first-principle calculations, although

¹Department of Physics, Zhejiang University, Hangzhou 310027, China; ²Anhui Province Key Laboratory of Condensed Matter Physics at Extreme Conditions, High Magnetic Field Laboratory, Chinese Academy of Sciences, Hefei 230031, China; ³HPCAT, Geophysical Laboratory, Carnegie Institution of Washington, Argonne, Illinois 60439, USA; ⁴State Key Laboratory of Silicon Materials, Zhejiang University, Hangzhou 310027, China and ⁵Collaborative Innovation Centre of Advanced Microstructures, Nanjing University, Nanjing 210093, China

Correspondence: Zhaorong Yang (zryang@issp.ac.cn) or Z-A. Xu (zhuana@zju.edu.cn)
These authors contributed equally: Yupeng Li, Chao An, Chenqiang Hua.

Received: 14 May 2018 Accepted: 24 October 2018

Published online: 19 November 2018

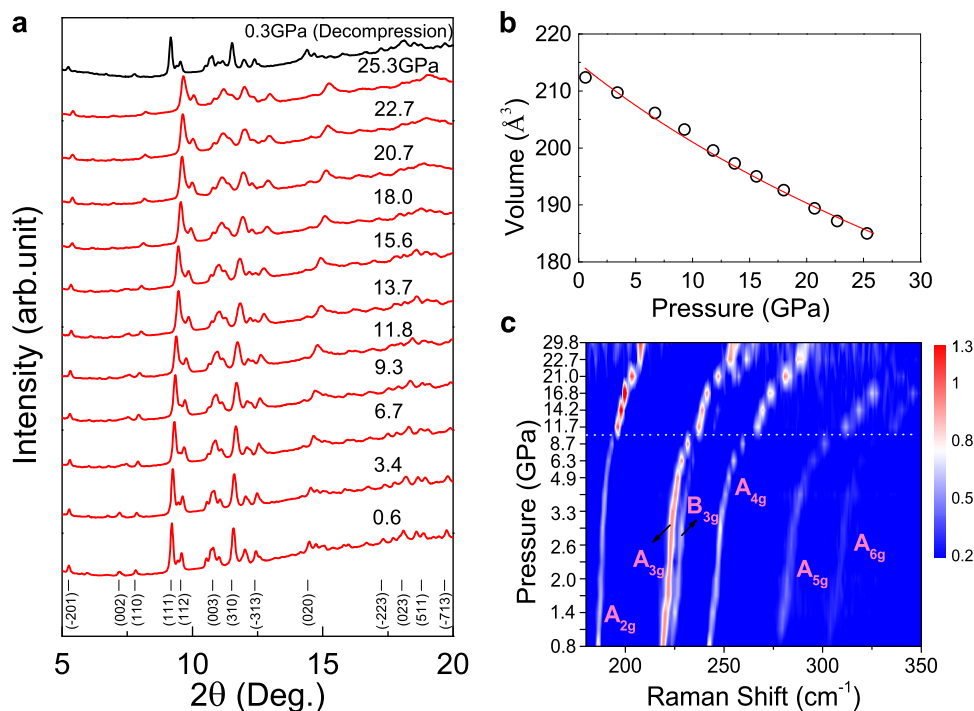


Fig. 1 High pressure structure of NbAs₂. **a** X-ray diffraction patterns of NbAs₂ at various pressures display no structural phase transition. **b** Unit-cell volume decreases with increasing pressure, while the volume diminishes by 13% at 25.3 GPa. **c** The Raman shifts at various pressures show the hardening and broadening of Raman scattering peaks

the electron–hole compensation under pressure is not so perfect. Instead, the dwindling of XMR and the emergence of SC are characterized by continuous Fermi surface change and gradual growth in density of state. Our results thus indicate the coexistence of XMR and SC. The growing density of states is usually beneficial to the occurrence of SC. Moreover, the Cooper pair formation in NbAs₂ may also be correlated to the enhanced electron–phonon coupling under high pressure, since the Raman studies reveal significant phonon mode hardening and broadening above 10 GPa. It is noteworthy that, in the SC region, the main hole pocket of NbAs₂ encloses the time-reversal-invariant (TRI) momenta M . These suggest NbAs₂ as a candidate of TRI topological superconductors.

RESULTS AND DISCUSSION

Pressure-dependent structure analysis

The structure evolution of NbAs₂ under pressure is determined by synchrotron radiation-based high-pressure XRD and Raman spectroscopy, as shown in Fig. 1. The XRD data are refined using the Rietveld method, and the Bragg peaks are well indexed by the space group $C2/m$ for both the 0.6 and 25.3 GPa data (See Supplementary Fig. S1). Within 30 GPa, the pressure-induced lattice changes are reversible. In Fig. 1a, we show the XRD results of NbAs₂ when the DAC is slowly decompressed from 29.8 to 0.3 GPa. The data are essentially identical to the bottom curve of 0.6 GPa. In Fig. 1b, the high pressure dependent unit-cell volumes can be fitted by the third-order Birch–Murnaghan equation of state,³⁷ and no distinct drop of the unit-cell volume is observed with the increase of pressure, which suggests stability of this structure. The monoclinic lattice is also manifested in pressure-dependent Raman scattering measurements, showing six fingerprinting peaks between 180 and 350 cm⁻¹, namely A_{2g}, A_{3g}, B_{3g}, A_{4g}, A_{5g}, and A_{6g}, respectively (see Fig. 1c). It is intriguing that Raman spectroscopy shows distinctive enhancement of A_{2g}, A_{3g}, B_{3g}, A_{4g}, and A_{5g} above 10 GPa, when the data are normalized by

the A_{2g} peak intensity. The distinct broadening in A_{2g}, A_{4g} and A_{5g}, which could be an indication of stronger electron–phonon coupling or pressure-enhanced defect scattering,³⁸ is also discernable above 10 GPa.

Resistivity measurements

Figure 2a, b summarize the resistance vs. temperature (R – T) characteristics of NbAs₂ at various pressures from 0.5 to 27.9 GPa. Below 9.8 GPa, NbAs₂ shows typical metallic behavior, which is characterized by monotonic increase in resistance with increasing temperature, and exhibits a lower residual-resistivity-ratio with enhancement of pressure. The trend is reversed at 9.8 GPa, when the whole R – T curve is upshifted by $\sim 0.03\Omega$ compared to 6.1 GPa. SC with a transition temperature of 2.63 K emerges at 12.8 GPa, but the resistance does not drop to zero even at 1.8 K (Fig. 2a). Further increase in pressure surprisingly starts to suppress T_c , although the SC transition becomes sharper, and zero-resistance behavior is observed at 16 GPa. Noticeably, the zero-resistance transition is accompanied by a positive resistance kink, which is very sharp and only extends within a temperature range of 0.2 K. Subsequently, the superconducting transition is gradually suppressed when the positive resistance kink becomes broader and its onset shifts to lower T . Above 23 GPa, the positive-resistance kink completely dominates.

In previous studies, the emergence of SC is generally accompanied with a suppression of the XMR effect in topological semimetals.^{14,15,39} There are different interpretations in the XMR suppression mechanism. Cai et al.³⁹ suggest that pressure weakens the electron–hole compensation in WTe₂ by gradually decreasing the hole carrier population. In situ pressure-dependent Hall measurements by Kang et al.¹⁴ indeed observe the change from a positive sign to negative sign in the Hall coefficients, suggesting increasing population of the electron carriers and decreasing hole carriers density. Moreover, Pan et al. report that the SC transition is induced by rapid increase in the density of states at the Fermi surface, as a result of the compression of the

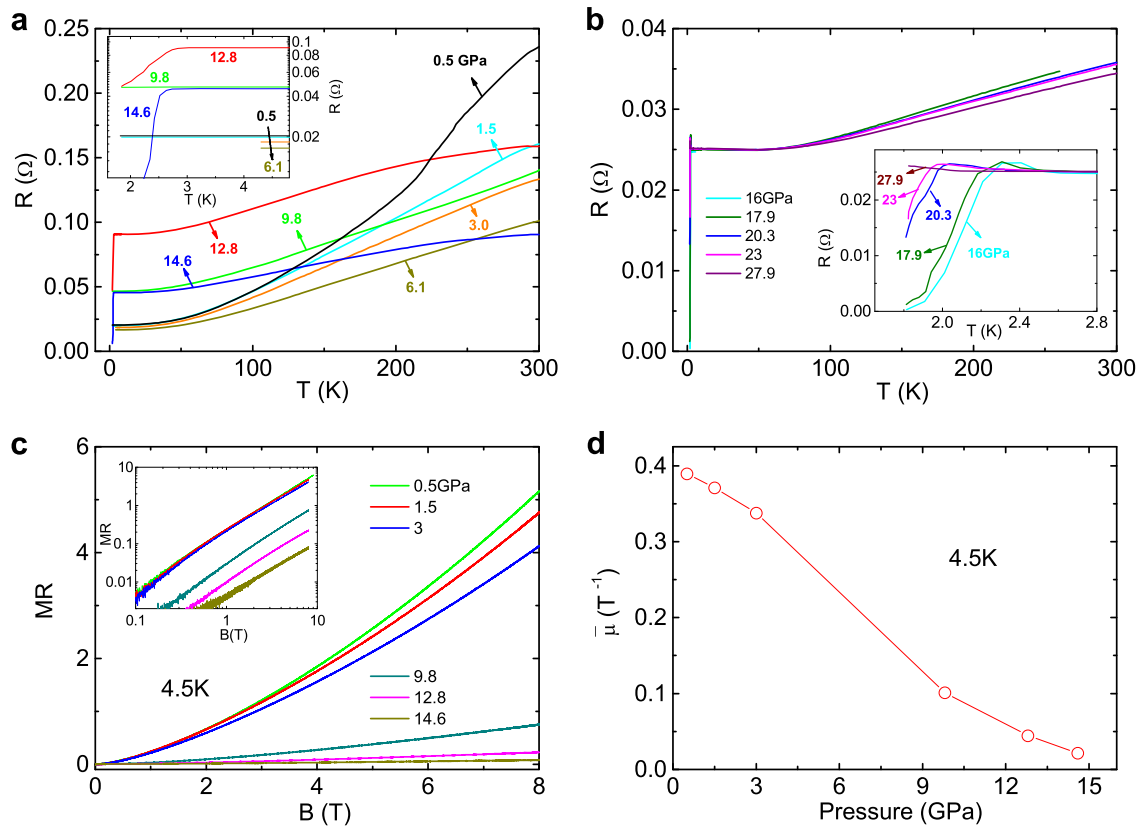


Fig. 2 Pressure-induced superconductivity in single-crystal NbAs₂. **a** Temperature-dependent resistance is measured from 0.5 to 14.6 GPa and superconducting transition appears at 12.8 GPa. The enlarged view of low temperature resistance is shown in the inset. **b** The resistance as a function of temperature at different pressures between 16 and 27.9 GPa is displayed with an enlarged plot around the superconducting transition in the inset. **c** Magnetoresistance (MR = (R(8T) - R(0T))/R(0T)) at 4.5 K is suppressed slowly as pressure increases from 0.5 to 14.6 GPa. The MR at 12.8 GPa and 8T is nearly 22%, which is still very large. **d** Average mobility $\bar{\mu}$ obtained by fitting to the formula $MR = (\bar{\mu}B)^{1.43}$ decreases monotonously with increasing pressure

unit cell,¹⁵ while the difference between hole pockets and electron pockets is enhanced with applied pressure.

NbAs₂ is a well compensated semimetal at ambient pressure.²⁸ When high pressure is applied, XMR at 8T is effectively suppressed from 5.16 at 0.5 GPa to 0.08 at 14.6 GPa, as shown in Fig. 2c. The dwindling of XMR as a function of pressure can be explained well by pressure-induced decrease in the average mobility $\bar{\mu}$,⁴⁰ using the power-law relation of $MR = (\bar{\mu}B)^l$. Using logarithmic scale (see the inset of Fig. 2c), it is clear that the XMR curves at different pressures have nearly the same linear slope ($l = 1.43$), which is a simple measure of the electron-hole compensation accuracy,³⁴ and the electron-hole compensation here is not so perfect. By fitting the experimental data to the aforementioned equation, we found that $\bar{\mu}$ decreases quasi-linearly as a function of pressure, and only shows a slight upward curvature as entering the SC region above 10 GPa (see Fig. 2d). Our results thus imply that a distinct phase boundary does not exist between SC and XMR, and the mechanism of SC in NbAs₂ may be different compared to other topological semimetals.¹⁴

The positive resistance kinks, which become broader and shift to lower temperature as a function of pressure (P), may be rooted in different mechanisms, such as superconductor to metal transition in disordered system,⁴¹ a probable foreshadow of p-wave SC in superconductor-ferromagnet nanowires structure,⁴² or highly anisotropic superconducting gap,⁴³ but should not be the same as the semiconductor-like behavior in LaO_{0.5}F_{0.5}BiSe₂.⁴⁴ When external magnetic field (B) is applied, T_c monotonically shifts to lower temperatures and the positive resistance kinks gradually become predominant. As shown in Fig. 3a, it is surprising that the

superconducting transition at 16 GPa is completely suppressed at 1000 Oe. This may be due to the predominant resistivity upturn, which pushes T_c to below 1.8 K. Nevertheless, with the available experimental data, we can define an empirical critical $T_c^{90\%}$ by those points at which R is 90% of the normal state, as seen in the inset of Fig. 3b. In Fig. 3b, the deduced $T_c^{90\%}$ can be well fitted by the Werthamer-Helfand-Hohenberg (WHH) model,⁴⁵ which yields the orbital-limited upper critical field in dirty-limited system by $H_{c2}^{orb}(0) \simeq -0.69T_c \times dH_{c2}/dT|_{T=T_c} = 2288$ Oe.

Interestingly, by plotting the pressure-dependent R at different T (4.5, 100, 200, and 300 K, respectively) in Fig. 3c, we are able to clearly see an anomaly at 12.8 GPa, which corresponds to the emergence of SC. However, there is no structural phase transition up to 29.8 GPa, so the origin of this behavior needs further investigation. By including the characteristic parameters of XMR, $T_c^{90\%}$ as a function of pressure, we can draw the P - T phase diagram for NbAs₂. As summarized in Fig. 3e, high pressure suppresses the XMR effect (the blue region) by reducing the average mobility $\bar{\mu}$. The emergence of SC may be related to the enhancement of density of states,^{15,46} and calculated density of states increase as a function of pressure, as seen in Fig. 3d. Moreover, there is a significant overlap between the XMR (the blue region) and SC region (the magenta region) when SC emerges at 12.8 GPa. Such a coexistence of XMR and SC is in contrast to the other cases like WTe₂ where XMR is significantly suppressed as entering the SC state under high pressure.¹⁴ Above 16 GPa, there is a probable phase competition between SC and the BM transition (the green region), which maybe lead to the vanishing of T_c at 27.9 GPa.

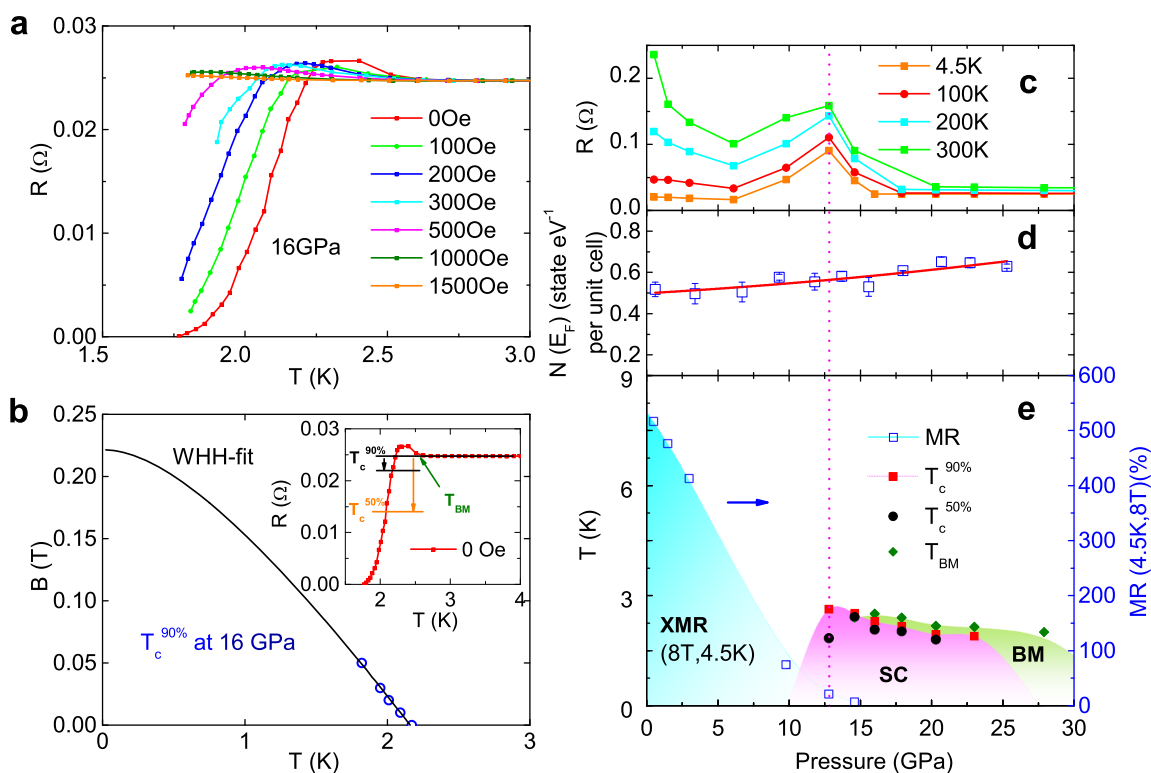


Fig. 3 Determination of upper critical field for superconductivity and temperature-pressure phase diagram of NbAs₂. **a** Temperature-dependent resistance at different magnetic fields is measured at 16 GPa. **b** H_{c2} as a function of temperature and its WHH fitting are displayed. The inset shows the definition of different superconducting transition temperatures and transition temperature of bad metal. **c** Resistance at 4.5, 100, 200, and 300 K in the normal state at different pressures shows the peak near 12.8 GPa where superconducting transition emerges. **d** Calculated density of states of NbAs₂ at the Fermi level vs. pressure. The squares are the density of states as a function of pressure, and the red line indicates the tendency of density of state under the pressure. **e** T_c is plotted against pressure as well as evolution of MR, and superconductivity appears at 12.8 GPa following the suppression of XMR with increasing pressure. The BM transition appears after 16 GPa. The regions of XMR, SC, and BM in the phase diagram are marked by blue, magenta, and green colors, respectively

Electronic structures under pressure

To get insights into the aforementioned experimental results, we have studied the pressure-dependent electronic structure of NbAs₂ using density-functional theory (DFT) calculations, which adopt the experimental lattice parameters determined by XRD. Figure 4 displays the DFT calculations at ambient pressure, 15.6, and 22.7 GPa, respectively. In excellent agreement with the XMR measurements, the DFT results confirm that pressure simultaneously increases electron and hole populations in NbAs₂, which is displayed in Fig. 4d–f where the electron pockets (magenta) and hole pockets (blue) all enlarge with increasing pressure. This is not surprising since the monoclinic lattice is retained under high pressure. Equally important, the steady growth in charge carrier does not show any anomaly, neither in density of states in Fig. 3d nor in Fermi surface topology, in the vicinity of 12.8 GPa when SC starts to emerge. According to the proposed theory by Fu et al.,²⁶ time-reversal-invariant topological SC in a centrosymmetry system requires odd-parity spin pairing and an Fermi surface enclosing an odd number of TRIM points. Although the pairing symmetry is not explicitly known, the latter condition is well satisfied in NbAs₂. As shown in Fig. 4, the main hole pocket of NbAs₂ enlarges under pressure, centering the TRIM point of M. In addition, the electronic specific-heat coefficient of $\gamma = 0.45$ mJ/mol/K² is observed from the specific heat measurements (see Fig. S3 in Supplementary Materials), suggesting weak electronic correlation in NbAs₂ at ambient pressure. With increasing pressure, the sudden hardening and broadening phonon modes may start to play a critical role in the emergence of SC, and the phonon-mediated pairing maybe

have an odd-parity symmetry in NbAs₂ if there is a singular behavior of the electron–phonon interaction at long wavelength.^{47,48} In addition, no structural transition is observed as entering the superconducting states with increasing pressure and thus the topological surface state should remain undisturbed at high pressure, which suggests the possibility of topologically superconducting surface states in NbAs₂ because of superconducting proximity effect.³ Therefore, NbAs₂ with time-reversal and inversion symmetries may be a candidate for topological superconductor. It is necessary to be checked by further experiments.

In summary, we study the high pressure-induced SC in topological semimetal NbAs₂, which shows a superconducting transition temperature of 2.63 K at 12.8 GPa. Unlike previously reported topological semimetals, no structural phase transition occurs near the superconducting region, which is supported both by the high-pressure synchrotron XRD and Raman data. Raman spectroscopy, resistance and specific heat data all suggest the critical importance of electron-phonon interactions on the SC pairing in NbAs₂, which may be a candidate of time-reversal-invariant topological superconductor with odd spin pairing parity. Strikingly, the SC phase emerges with a nearly invariable electron-hole compensation and shows no anomaly in the density of states in the vicinity of the critical pressure of 12.8 GPa. Our results illustrate that high-pressure induced SC may be more complex in physical origins than the prevailing explanations, and the monoclinic family of MPn₂ may provide a platform to test various theoretical proposals and to search for topological SC.

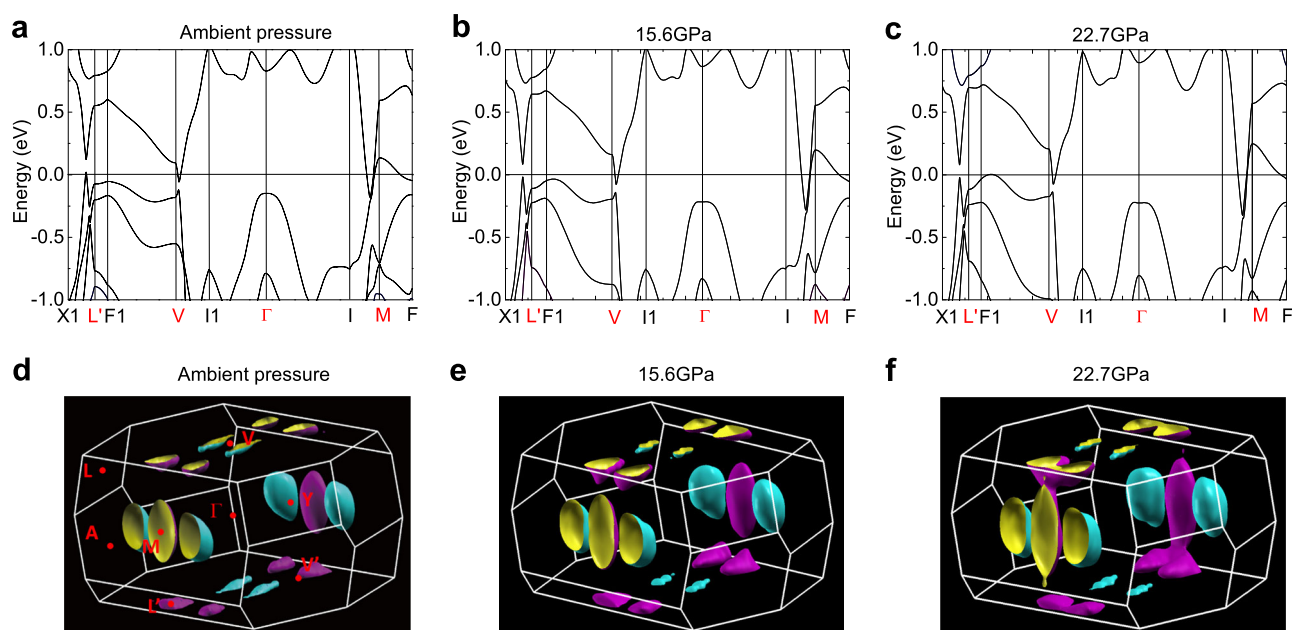


Fig. 4 Pressure-dependent band structures of NbAs₂, showing increasing electron and hole pockets. **a–c** Band structures in NbAs₂ are shown at ambient pressure, 15.6 and 22.7 GPa, respectively. The red points are TRIM points. **d–f** 3D Fermi surface diagram at ambient pressure, 15.6 and 22.7 GPa indicates that the TRIM (M) is enclosed by the hole-type Fermi surface (the magenta pockets), and blue pockets are electron-type Fermi surface. TRIM points are marked in the Fig. 4d

METHODS

Samples and experimental technique

Single crystals of NbAs₂ were grown by means of a vapor transport technique.²⁸ High pressure was generated by a screw-pressure-type DAC consisting of nonmagnetic Cu–Be alloy and two diamonds with the culet of 300 μm diameter. A T301 stainless-steel gasket with a 280 μm diameter hole was used for different runs of high-pressure resistance measurement by the standard four-probe method. The single crystal was placed in the hole and a mixture of fine cubic boron nitride powder with epoxy was compressed firmly to insulate the electrodes from the gasket. Pressure medium was daphne 7373 oil and some ruby powder was applied to demarcate the pressure by the ruby fluorescence method at room temperature. High-pressure synchrotron powder XRD ($\lambda = 0.4246 \text{ \AA}$) was performed at room temperature at the beamline 16 BM-D,⁴⁹ High Pressure Collaborative Access Team (HPCAT).

DFT calculations

The electron structure calculations were performed with the Vienna ab initio simulation package^{50,51} by the method of the projector augmented wave⁵² and the generalized gradient approximation⁵³ in order to introduce the exchange–correlation potential. Spin–orbit coupling has been included using the second variation perturbation method.⁵⁴ In addition, the plane-wave cutoff energy is setting about 500 eV and $21 \times 21 \times 13$ k-points sampling is performed based on the Monkhorst–Pack scheme.⁵⁵ The total energy is ensured to be converged within 10^{-6} eV. We use the structure parameters of high-pressure synchrotron XRD to relax the structure with the tolerance of 0.01 eV/Å³

DATA AVAILABILITY

The data that support the findings of this study are available from the corresponding author upon reasonable request.

ACKNOWLEDGMENTS

This work was supported by the National Key R&D Program of China (Grant nos. 2016YFA0300204, 2016YFA0300402, and 2017YFA0303002), the National Basic Research Program of China (Grant no. 2014CB921203), and the National Science Foundation of China (Grant nos. U1332209, 11574264, and 11774305). Y.Z. acknowledges the start funding support from the Thousand Talents Plan. The X-ray work was performed at HPCAT (Sector 16), Advanced Photon Source, Argonne

National Laboratory. HPCAT operations are supported by DOE–NNSA under Award No. DE–NA0001974 and DOE–BES under Award No. DE–FG02–99ER45775, with partial instrumentation funding by NSF. The Advanced Photon Source is a US Department of Energy (DOE) Office of Science User Facility operated for the DOE Office of Science by Argonne National Laboratory under Contract No. DE–AC02–06CH11357.

AUTHOR CONTRIBUTIONS

Y.P. Li synthesized and characterized the single crystals. C. An, Y.H. Zhou, and Z.R. Yang conducted the high-pressure transport measurements. Y. Zhou, C. An, and R.R. Zhang carried out the Raman experiments, X.L. Chen and C.Y. Park performed the high-pressure synchrotron X-ray diffraction experiments. C.Q. Hua and Y.H. Lu did the DFT calculations. Y.P. Li, C.Q. Hua, Y.H. Lu, Z.R. Yang, Y. Zheng, and Z.A. Xu wrote the paper. All the authors analyzed the data and discussed the results. Y.P. Li, C. An, and C.Q. Hua were co-first authors to this work. Z.R. Yang and Z.A. Xu co-supervised the project.

ADDITIONAL INFORMATION

Supplementary information accompanies the paper on the *npj Quantum Materials* website (<https://doi.org/10.1038/s41535-018-0132-1>).

Competing interests: The authors declare no competing interests.

Publisher's note: Springer Nature remains neutral with regard to jurisdictional claims in published maps and institutional affiliations.

REFERENCES

- Nayak, C., Simon, S. H., Stern, A., Freedman, M. & Das Sarma, S. Non-abelian anyons and topological quantum computation. *Rev. Mod. Phys.* **80**, 1083–1159 (2008).
- Wilczek, F. Majorana returns. *Nat. Phys.* **5**, 614–618 (2009).
- Fu, L. & Kane, C. L. Superconducting proximity effect and Majorana fermions at the surface of a topological insulator. *Phys. Rev. Lett.* **100**, 096407 (2008).
- Xu, J. P. et al. Experimental detection of a Majorana mode in the core of a magnetic vortex inside a topological insulator–superconductor Bi₂Te₃/NbSe₂ heterostructure. *Phys. Rev. Lett.* **114**, 017001 (2015).
- Sun, H. H. et al. Majorana zero mode detected with spin selective andreev reflection in the vortex of a topological superconductor. *Phys. Rev. Lett.* **116**, 257003 (2016).

6. Sau, J. D., Lutchyn, R. M., Tewari, S. & Sarma, S. D. Generic new platform for topological quantum computation using semiconductor heterostructures. *Phys. Rev. Lett.* **104**, 040502 (2010).
7. Lutchyn, R. M., Sau, J. D. & Sarma, S. D. Majorana fermions and a topological phase transition in semiconductor–superconductor heterostructures. *Phys. Rev. Lett.* **105**, 077001 (2010).
8. Nadj-Perge, S. et al. Observation of Majorana fermions in ferromagnetic atomic chains on a superconductor. *Science* **346**, 602–607 (2014).
9. Qi, X. L., Hughes, T. L. & Zhang, S. C. Chiral topological superconductor from the quantum Hall state. *Phys. Rev. B* **82**, 184516 (2010).
10. Chung, S. B., Qi, X. L., Maciejko, J. & Zhang, S. C. Conductance and noise signatures of Majorana backscattering. *Phys. Rev. B* **83**, 100512(R) (2011).
11. Wang, J., Zhou, Q., Lian, B. & Zhang, S. C. Chiral topological superconductor and half-integer conductance plateau from quantum anomalous Hall plateau transition. *Phys. Rev. B* **92**, 064520 (2015).
12. He, Q. L. et al. Chiral Majorana fermion modes in a quantum anomalous Hall insulator–superconductor structure. *Science* **357**, 294–299 (2017).
13. Qi, Y. et al. Superconductivity in Weyl semimetal candidate MoTe_2 . *Nat. Commun.* **7**, 11038 (2015).
14. Kang, D. et al. Superconductivity emerging from a suppressed large magnetoresistant state in tungsten ditelluride. *Nat. Commun.* **6**, 7804 (2015).
15. Pan, X. C. et al. Pressure-driven dome-shaped superconductivity and electronic structural evolution in tungsten ditelluride. *Nat. Commun.* **6**, 7805 (2015).
16. He, L. P. et al. Pressure-induced superconductivity in the three-dimensional Dirac semimetal Cd_3As_2 . *NPJ Quantum Mater.* **1**, 16014 (2016).
17. Zhou, Y. H. et al. Pressure-induced superconductivity in a three-dimensional topological material ZrTe_5 . *Proc. Natl Acad. Sci. USA* **113**, 2904–2909 (2016).
18. Kirshenbaum, K. et al. Pressure-induced unconventional superconducting phase in the topological insulator Bi_2Se_3 . *Phys. Rev. Lett.* **111**, 087001 (2013).
19. Zhang, J. L. et al. Pressure-induced superconductivity in topological parent compound Bi_2Te_3 . *Proc. Natl Acad. Sci. USA* **108**, 24–28 (2011).
20. Zhu, J. et al. Superconductivity in topological insulator Sb_2Te_3 induced by pressure. *Sci. Rep.* **3**, 2016 (2013).
21. Wang, H. et al. Observation of superconductivity induced by a point contact on 3D Dirac semimetal Cd_3As_2 crystals. *Nat. Mater.* **15**, 38 (2016).
22. Wang, H. et al. Discovery of tip induced unconventional superconductivity on Weyl semimetal. *Sci. Bull.* **62**, 425–430 (2017).
23. Hor, Y. S. et al. Superconductivity in $\text{Cu}_x\text{Bi}_2\text{Se}_3$ and its implications for pairing in the undoped topological insulator. *Phys. Rev. Lett.* **104**, 057001 (2010).
24. Shruti, Maurya, Neha, V. K., Srivastava, P. & Patnaik, S. Superconductivity by Sr intercalation in the layered topological insulator Bi_2Se_3 . *Phys. Rev. B* **92**, 020506 (2015).
25. Qi, X. L., Hughes, T. L., Raghu, S. & Zhang, S. C. Time-reversal-invariant topological superconductors and superfluids in two and three dimensions. *Phys. Rev. Lett.* **102**, 187001 (2009).
26. Fu, L. & Berg, E. Odd-parity topological superconductors: Theory and application to $\text{Cu}_x\text{Bi}_2\text{Se}_3$. *Phys. Rev. Lett.* **105**, 097001 (2010).
27. Li, Y. K. et al. Resistivity plateau and negative magnetoresistance in the topological semimetal TaSb_2 . *Phys. Rev. B* **94**, 121115(R) (2016).
28. Li, Y. P. et al. Negative magnetoresistance in topological semimetals of transition-metal dipnictides with nontrivial Z_2 indices. *arXiv:1603.04056* (2016).
29. Shen, B., Deng, X. Y., Kotliar, G. & Ni, N. Fermi surface topology and negative longitudinal magnetoresistance observed in the semimetal NbAs_2 . *Phys. Rev. B* **93**, 195119 (2016).
30. Wu, D. S. et al. Giant semiclassical magnetoresistance in high mobility TaAs_2 semimetal. *Appl. Phys. Lett.* **108**, 042105 (2016).
31. Luo, Y. K. et al. Anomalous electronic structure and magnetoresistance in TaAs_2 . *Sci. Rep.* **6**, 27294 (2016).
32. Yuan, Z. J., Lu, H., Liu, Y. J., Wang, J. F. & Jia, S. Large magnetoresistance in compensated semimetals TaAs_2 and NbAs_2 . *Phys. Rev. B* **93**, 184405 (2016).
33. Wang, Y. Y., Yu, Q. H., Guo, P. J., Liu, K. & Xia, T. L. Resistivity plateau and extremely large magnetoresistance in NbAs_2 and TaAs_2 . *Phys. Rev. B* **94**, 041103 (2016).
34. Wang, Z. et al. Topological phase transition induced extreme magnetoresistance in TaSb_2 . *arXiv:1603.01717* (2016).
35. Xu, C. C. et al. Electronic structures of transition metal dipnictides XPn_2 ($\text{X} = \text{Ta}, \text{Nb}; \text{Pn} = \text{P}, \text{As}, \text{Sb}$). *Phys. Rev. B* **93**, 195106 (2016).
36. Gresch, D., Wu, Q., Winkler, G. W. & Soluyanov, A. A. Hidden Weyl points in centrosymmetric paramagnetic metals. *New J. Phys.* **19**, 035001 (2017).
37. Birch, F. Finite elastic strain of cubic crystals. *Phys. Rev.* **71**, 809–824 (1947).
38. Jin, F. et al. Raman scattering study of large magnetoresistance semimetals TaAs_2 and NbAs_2 . *Phys. Rev. B* **94**, 094302 (2016).
39. Cai, P. L. et al. Drastic pressure effect on the extremely large magnetoresistance in WTe_2 : quantum oscillation study. *Phys. Rev. Lett.* **115**, 057202 (2015).
40. Zhu, Z. W. et al. Quantum oscillations, thermoelectric coefficients, and the Fermi surface of semimetallic WTe_2 . *Phys. Rev. Lett.* **114**, 176601 (2015).
41. Xing, Y. et al. Quantum Griffiths singularity of superconductor-metal transition in Ga thin films. *Science* **350**, 542–545 (2015).
42. Wang, J. et al. Interplay between superconductivity and ferromagnetism in crystalline nanowires. *Nat. Phys.* **6**, 389–394 (2010).
43. Du, G. et al. Superconductivity with two-fold symmetry in topological superconductor $\text{Sr}_3\text{Bi}_2\text{Se}_3$. *Sci. China Phys. Mech. Astron.* **60**, 037411 (2017).
44. Liu, J. Z., Li, S., Li, Y. F., Zhu, X. Y. & Wen, H. H. Pressure-tuned enhancement of superconductivity and change of ground state properties in $\text{La}_{0.5}\text{F}_{0.5}\text{BiSe}_2$ single crystals. *Phys. Rev. B* **90**, 094507 (2014).
45. Werthamer, N. R., Helfand, E. & Hohenberg, P. C. Temperature and purity dependence of the superconducting critical field, H_{c2} . III. electron spin and spin–orbit effects. *Phys. Rev.* **147**, 295–302 (1966).
46. Ueno, K. et al. Discovery of superconductivity in KTaO_3 by electrostatic carrier doping. *Nat. Nanotechnol.* **6**, 408–412 (2011).
47. Wan, X. G. & Savrasov, S. Y. Turning a band insulator into an exotic superconductor. *Nat. Commun.* **5**, 4144 (2014).
48. Brydon, P. M. R., Das Sarma, S., Hui, H. Y. & Sau, J. D. Odd-parity superconductivity from phonon-mediated pairing: application to $\text{Cu}_x\text{Bi}_2\text{Se}_3$. *Phys. Rev. B* **90**, 184512 (2014).
49. Park, C. Y. et al. New developments in micro-X-ray diffraction and X-ray absorption spectroscopy for high-pressure research at 16-BM-D at the advanced photon source. *Rev. Sci. Instrum.* **86**, 072205 (2015).
50. Kresse, G. & Hafner, J. Ab initio molecular dynamics for liquid metals. *Phys. Rev. B* **47**, 558–561 (1993).
51. Kresse, G. & Furthmüller, J. Efficient iterative schemes for ab initio total-energy calculations using a plane-wave basis set. *Phys. Rev. B* **54**, 11169–11186 (1996).
52. Kresse, G. & Joubert, D. From ultrasoft pseudopotentials to the projector augmented-wave method. *Phys. Rev. B* **59**, 1758–1775 (1999).
53. Perdew, J. P., Burke, K. & Ernzerhof, M. Generalized gradient approximation made simple. *Phys. Rev. Lett.* **77**, 3865–3868 (1996).
54. Koelling, D. D. & Harmon, B. N. A technique for relativistic spin-polarised calculations. *J. Phys. C* **10**, 3107–3114 (1977).
55. Monkhorst, H. J. & Pack, J. D. Special points for Brillouin-zone integrations. *Phys. Rev. B* **13**, 5188–5192 (1976).



Open Access This article is licensed under a Creative Commons

Attribution 4.0 International License, which permits use, sharing, adaptation, distribution and reproduction in any medium or format, as long as you give appropriate credit to the original author(s) and the source, provide a link to the Creative Commons license, and indicate if changes were made. The images or other third party material in this article are included in the article's Creative Commons license, unless indicated otherwise in a credit line to the material. If material is not included in the article's Creative Commons license and your intended use is not permitted by statutory regulation or exceeds the permitted use, you will need to obtain permission directly from the copyright holder. To view a copy of this license, visit <http://creativecommons.org/licenses/by/4.0/>.

© The Author(s) 2018